46th AIAA Aerospace Sciences Meeting and Exhibit
7 - 10 January 2008, Reno, Nevada

AIAA 2008-777

A High-Order Residual-Distribution Scheme with Variation-Bounded Nonlinear Stabilization

S. M. J. Guzik* and C. P. T. Groth†

University of Toronto Institute for Aerospace Studies

4925 Dufferin Street, Toronto, Ontario, M3H 5T6, Canada

A high-order implementation of a residual-distribution scheme is proposed with a new mechanism for enforcing nonlinear stability. Modern second-order accurate residual distribution methods satisfy a positivity condition to achieve nonlinear stability in the vicinity of unresolved gradients. While this approach is very effective at capturing discontinuities, a degradation in accuracy and spatial order of convergence can occur for smooth flows. Additionally, the best non-linear techniques have proven difficult to extend to systems of equations. High-order (beyond second-order) implementations of the residual-distribution method provide more information about the local variation of the solution. This extra information is used to implement a steady and element-local analogy to the nonlinear stability condition of bounded total-variation. Essentially, the scheme examines the variation in the solution and selectively applies the positivity condition only in mesh elements where the variation is deemed to be too high. Steady solutions of scalar equations in two-dimensions illustrate that the method shows potential for recovering the desired accuracy in smooth regions while satisfactorily damping oscillations near discontinuities.

I. Introduction

RESIDUAL-distribution ($\mathcal{RD}$) methods attempt to improve the accuracy of multidimensional solutions to hyperbolic partial differential equations with respect to current techniques such as the Godunov-type finite-volume ($\mathcal{FV}$) method. There is some dissatisfaction with $\mathcal{FV}$ methods because the process for extending a physical and rather elegant one-dimensional Godunov scheme to multiple dimensions is to apply the one-dimensional scheme in multiple directions. In this process, the splitting of the flux becomes biased in directions normal to the faces of the computational cells and the schemes are no longer quite as physical. Desirable numerical properties, such as nonlinear stability, also simply inherit (possibly excessively) from the one-dimensional scheme. Although this dimensional splitting has been proven to work quite well in practice, improvements can be made. As shown by Roe and Sidilkover,[1] dimensional splitting is about the worst technique one can use for first-order solutions. Residual distribution methods attempt to correct this deficiency by explicitly modelling the underlying multidimensional physics.

One of the main advantages of the $\mathcal{RD}$ method is that it features a multidimensional positivity property.[2] The first-order positive formulation also features much less numerical diffusion than first-order dimensionally-split Godunov-type schemes.[1] Consequently, it is a very effective method for capturing discontinuities. The improved resolution of discontinuities as compared to $\mathcal{FV}$ methods has been illustrated in previous studies for both steady[3–5] and unsteady[6,7] flows.

Unfortunately, extending the positive linear distribution schemes such that they are also linearity-preserving (and can therefore produce second-order solutions in smooth regions) has proven challenging. Solutions of smooth flows obtained with a nonlinear (second-order and monotone) formulation can exhibit much less accuracy than linear (second-order and non-monotone) formulations. More importantly, the spatial order-of-convergence can degrade significantly below second-order for the nonlinear formulation. The exact mechanism behind the degradation of spatial convergence is not fully understood but it would seem to be related to the behaviour of some limiters in smooth regions. While a method that does not degrade

*PhD Candidate, Email: sguzik@utias.utoronto.ca, Student Member AIAA
†Associate Professor, Email: groth@utias.utoronto.ca, Senior Member AIAA

in accuracy is known (and will be presented), it has proven difficult to extend it to systems of equations. In this work, the problem of degraded accuracy is approached from a different perspective, by examining the variation of the solution to provide the non-linear coupling necessary for a scheme that is both monotone and linearity-preserving. The positive nonlinear stability condition of current $\mathcal{RD}$ schemes is thereby weakened by only applying it in selected elements.

Inspired by $\mathcal{FV}$ methods, which achieve nonlinear stability by examining the shape of a reconstructed solution over several cells,[8] a similar approach is sought for the $\mathcal{RD}$ method. The proposed formulation, analogous to a total-variation-bounded scheme and specifically labeled *element-variation-bounded (EVB) scheme* from here on, makes use of an interpolation that encompasses several elements. The extra information from the expanded stencil is also used to increase the spatial order-of-accuracy. The compact stencil inherent to the $\mathcal{RD}$ method is retained since the high-order reconstructions only use the minimum number of vertices necessary to complete the interpolation.

There are two primary motivations for this work. The first is the argument that, in the vicinity of discontinuities, the interpolation of the solution must be linear. It is not sufficient to merely use a monotone distribution scheme. This argument will be supported by the numerical results to follow. The second motivation is to circumvent the lack of accurate, monotone, and stable $\mathcal{RD}$ schemes for solving systems of equations such as the Euler equations. The proposed technique for detecting large unresolved gradients would allow for the application of monotone nonlinear $\mathcal{RD}$ schemes only in those regions and highly-accurate linear $\mathcal{RD}$ schemes elsewhere.

The paper is organized as follows. In section II, fundamentals of the residual distribution method are presented along with the method of high-order construction. Deficiencies of positive $\mathcal{RD}$ formulations are illustrated by second-order solutions to smooth scalar flows. In section III, the EVB scheme is conceptualized in one dimension before being extended to multiple dimensions. Enhancements to the scheme based on numerical observations are also presented. Details of the numerical method are presented in section IV. Application of the EVB scheme is shown in section V for both smooth and discontinuous flows.

II. $\mathcal{RD}$ Methods for Scalar Advection

Residual distribution methods calculate the residual (or fluctuation) on an element, E, of an unstructured mesh and then, by some appropriate method, distribute the fluctuation to the nodes of that element to advance the solution in time. Residual distribution methods are cell-vertex methods that are usually solved on simplexes (triangles in two space dimensions).

For the scalar advection equation, one has

$$\frac{\partial u}{\partial t} + \sum_{j=1}^{d} \left(\lambda_j \frac{\partial u}{\partial x_j} \right) = 0 \,, \tag{1}$$

where d is the number of dimensions and λ_j is the advection speed in the jth coordinate direction. The fluctuation on a simplex element, E, is defined as

$$\begin{aligned} \phi^E &= -\int_E \frac{\partial u}{\partial t} d\Omega_E = \int_E \sum_{j=1}^{d} \left(\lambda_j \frac{\partial u}{\partial x_j} \right) d\Omega_E \\ &= \left[\sum_{j=1}^{d} \left(\bar{\lambda}_j \hat{x}_j \right) \right] \cdot \int_E \vec{\nabla} u \, d\Omega_E \,, \end{aligned} \tag{2}$$

where Ω_E is the element area, $\hat{x}_j$ defines a unit vector in the jth coordinate direction, and $\bar{\lambda}_j$ is linearized over the element. For non-linear equations, $\bar{\lambda}_j$ is determined via a conservative linearization such that

$$\left[\sum_{j=1}^{d} \left(\bar{\lambda}_j \hat{x}_j \right) \right] \cdot \int_E \vec{\nabla} u \, d\Omega_E = -\oint_{\partial E} \vec{F}(u) \cdot \hat{n} \, d\mathcal{S} \,, \tag{3}$$

where $\hat{n}$ is the inwards-pointing unit normal vector of surface element $d\mathcal{S}$. For second-order schemes, the solution, u, is assumed to vary linearly in the element. The integral in Eq. (2) can then be evaluated exactly

to obtain

$$\phi^E = \left[\sum_{j=1}^{d} \left(\bar{\lambda}_j \hat{x}_j\right)\right] \cdot \frac{1}{d} \sum_{i=1, i\in E}^{d+1} u_i \vec{n}_i = \sum_{i=1, i\in E}^{d+1} k_i u_i \,. \tag{4}$$

The index i loops over each node of an element and the vector $\vec{n}_i$ defines the inwards normal of the edge opposite node i and scaled by the length of the edge. The *inflow parameters*, k_i, are defined by

$$k_i = \frac{1}{d}\left[\sum_{j=1}^{d} \left(\bar{\lambda}_j \hat{x}_j\right)\right] \cdot \vec{n}_i \,, \tag{5}$$

and describe whether edge i sees the inflow (positive) or outflow (negative) of the solution quantity. Because $\bar{\lambda}_j$ is linearized, $\sum_{i=1, i\in E}^{d+1} k_i = 0$.

The distribution of the fluctuation to the nodes, ϕ_i^E, is governed by distribution coefficients, β_i, with $\phi_i^E = \beta_i \phi^E$ and, for consistency, $\sum_{i, i\in E}^{d+1} \beta_i = 1$. The nodal residual is defined as the sum of all fluctuations distributed to node i from all elements, E, that share node i as a vertex. The semi-discrete update formula is then

$$\Omega_i \frac{\mathrm{d}u_i}{\mathrm{d}t} + \sum_E \beta_i^E \phi^E = 0 \,, \tag{6}$$

where Ω_i is the area of the dual mesh, shown in Fig. 1, associated with node i of the unstructured mesh. Various time-marching schemes can be applied to the solution of the ordinary differential equations for the nodal values of the solution. An explicit-Euler algorithm is used for the results herein.

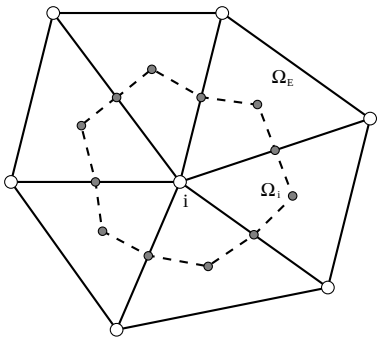

Figure 1. Primary elements (solid lines) and dual mesh (dashed lines) created from element centroids and edge midpoints.

There exist many formulae for defining the distribution coefficients, β_i, each of which leads to a scheme with different characteristics. Some common schemes and their key properties are listed in Table 1. Schemes that are positive ($\mathcal{P}$) are monotonicity-preserving while those that are linearity-preserving ($\mathcal{LP}$) achieve higher-orders of accuracy (second-order for a linear interpolation of the fluctuation). It is sufficient that the distribution coefficients are bounded for a scheme to be $\mathcal{LP}$.[2]

Table 1. Properties of $\mathcal{RD}$ Schemes

Scheme	*Linearity*	$\mathcal{P}$	$\mathcal{LP}$
N	linear	✓	
LDA	linear		✓
LN	non-linear	✓	✓
B	non-linear	✓[a]	✓

[a] Positivity has not been formally demonstrated but is usually assumed based on numerical results.

The N schemes is a linear first-order scheme that is formulated to ensure positivity.[9,10] The fluctuation distributed to each vertex is computed by

$$\phi_i^N = k_i^+ \left(u_i - u_{in}\right) \,, \tag{7}$$

where

$$u_{in} = \frac{\sum_{j=1, j\in E}^{d+1} k_j^- u_j}{\sum_{j=1, j\in E}^{d+1} k_j^-} \,. \tag{8}$$

The distribution coefficients for the N scheme are not bounded and may tend to $\pm\infty$ as $\phi^E \to 0$.

The LN scheme is constructed from the N scheme but recovers property $\mathcal{LP}$ by limiting the distribution coefficients when one of them becomes negative. Use of a minmod limiter produces a scheme identical to the positive-streamwise-invariant (PSI) scheme of Struijs[11] that is often quoted in the literature.[12]

The LDA scheme is a linear scheme that ensures $\mathcal{LP}$ but has no mechanism for enforcing nonlinear stability. The distribution is governed by the location at which the linearized characteristic vector intersects the outflow edge. In Fig. 2, $\beta_i = L_i/L$ and $\beta_j = L_j/L$. This is more conveniently expressed as

$$\beta_i^{LDA} = -\frac{k_i^+}{\sum_{j=1,j\in E}^{d+1} k_j^-}\,. \tag{9}$$

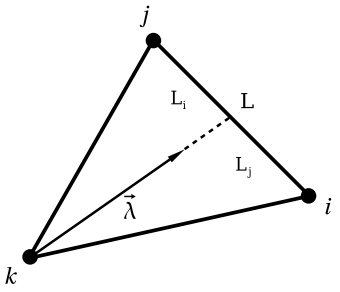

Figure 2. The LDA distribution is governed by the location $\bar{\lambda}$ intersects the outflow edge.

The blended scheme is a blending of the N and LDA schemes, $\phi^B = \theta\phi^N + (1-\theta)\phi^{LDA}$. There are several possible definitions of the blending coefficient θ; see Abgrall[3] for a definition that reproduces the PSI scheme. In this work, the heuristic definition proposed by Deconinck et al.,[2]

$$\theta = \frac{\left|\phi^E\right|}{\sum_{l=1,l\in E}^{d+1} \left|\phi_l^N\right| + \epsilon}\,, \qquad \epsilon = 10^{-10}\,, \tag{10}$$

is used where θ is defined to switch to the LDA scheme when divergence of the nodal fluctuation, as computed by the N-scheme, is detected. Positivity of this particular blended scheme has not been formally proven. However, it has been shown (and will be demonstrated herein) to have essentially the same behaviour as the PSI scheme which is positive. For simplicity of the discussion, the B scheme will be subsequently referred to as positive. The blended scheme is introduced here because it provides a convenient mechanism for selecting either an N or LDA scheme. In smooth regions, θ can be explicitly set to 0 to mandate use of the LDA scheme.

II.A. Accuracy of Residual Distribution Schemes

The spatial order of accuracy is demonstrated by plotting the L_1-error norms of the solution with respect to the square root of the number of grid points N_D (i.e., the dimensional spacing of the computational grid). The variation of the error as a function of N_D is expected to have the form

$$L_1\text{-error} = \alpha {N_D}^{\beta}\,, \tag{11}$$

where α describes the absolute magnitude of the error and β describes the order of convergence.

Figure 3 illustrates the accuracy of various second-order $\mathcal{RD}$ distribution schemes and a second-order Godunov-type $\mathcal{FV}$ scheme for the circular advection of a smooth exponential profile. While both the LDA distribution scheme and the $\mathcal{FV}$ scheme have similar orders of convergence, the absolute error (α in Eq. (11)) of the LDA scheme is almost an order of magnitude less than that of the $\mathcal{FV}$ scheme. The PSI and blended distribution schemes, on the other hand, have similar absolute error to the $\mathcal{FV}$ method, and, disconcertingly, an order of convergence that is less than second order. On finer meshes, the $\mathcal{FV}$ method becomes more accurate than the PSI and

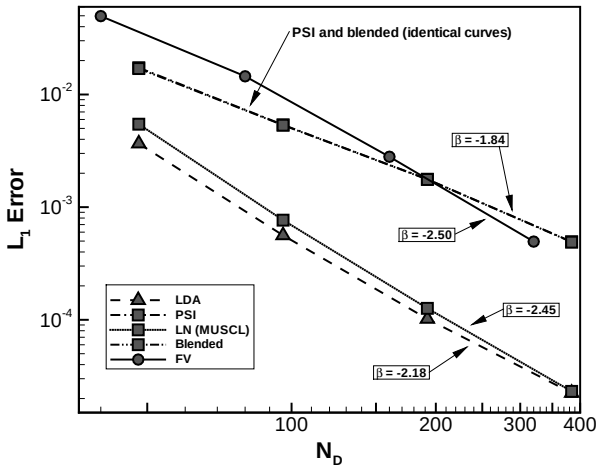

Figure 3. L_1-error as a function of mesh density for circular advection.

blended schemes. It would be highly desirable to have a monotonicity-preserving scheme that instead closely follows the LDA curve. One way this can be achieved is by using a MUSCL limiter[8] of the form

$$\Psi(r) = \max\left[0, \min\left(2r, \frac{r+1}{2}, 2\right)\right]. \tag{12}$$

The enhanced performance of the MUSCL limiter is thought to be related to the behaviour of the limiter near $r \approx 1$.[13]

To fully retain the benefits to accuracy provided by the $\mathcal{RD}$ method, it would seem necessary to use the LN (MUSCL) scheme for flows that may contain discontinuities. Unfortunately, it is difficult to extend the LN (MUSCL) scheme to the Euler equations. The best known approach at solving systems of equations is to perform a hyperbolic/elliptic splitting.[2, 5, 10, 14, 15] This decouples the system into four scalar equations for supersonic flows and two scalar equations plus an acoustic subset for subsonic flows. With this approach, the scalar equations may be solved using the LN (MUSCL) scheme (the theses by Mesaros[14] and Rad[15] provide two techniques for solving the acoustic subset) but the entire system suffers from a degeneracy in the system eigenvectors in stagnation regions. Another approach to solving systems, that of matrix distribution,[2, 5, 16] works well with matrix versions of the LDA and blended schemes. Unfortunately, matrix distribution tends to suffer from instabilities in smooth regions when mapped distribution schemes[17, 18] (basically extensions of the LN scheme that are easier to apply to matrix distribution) are used. Abgrall[19] has performed an analysis of this instability and proposed a fix involving the addition of artificial dissipation. The high-order approach developed herein allows for explicit detection of large gradients. In smooth regions, the highly accurate LDA scheme can be used. In regions with large gradients, the blended scheme can be applied to ensure monotonicity. This approach circumvents the need to find an accurate, monotone, and stable distribution scheme for all flow regions. The effectiveness of such an approach is examined in this paper for scalar equations.

II.B. Construction of High-Order Schemes

Schemes with an order of accuracy greater than two are constructed by following a framework similar to that of finite-element theory. Abgrall and Roe[17] used such an approach to increase the number of degrees of freedom in an element by inserting nodes in the interior. This leads to the construction of P^2 and P^3 elements for third and fourth order solutions, respectively. In this work, an inverse approach is taken where *reconstruction elements* are defined as an ordered collection of *primary elements* with the desired degrees of freedom. Figure 4 shows a reconstruction element with 9 primary elements and 10 degrees of freedom (vertices) for a fourth order solution. Although the primary elements should have an arrangement similar to that shown in Fig. 4, the reconstruction elements can have a completely unstructured connectivity. The differences from the approach of Abgrall and Roe[17] are purely ideological. Note that alternative approaches to constructing high-order $\mathcal{RD}$ schemes do exist in the literature.[20–22]

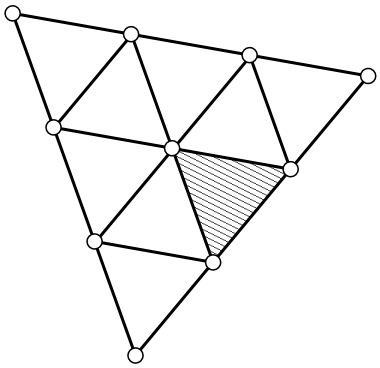

Figure 4. Fourth order reconstruction element consisting of an ordered collection of primary elements (shaded).

Lagrange basis functions are used to define a high-order interpolating polynomial for the entire reconstruction element. Within a reconstruction element, both the coordinates and the solution are interpolated by the Lagrange basis functions. These polynomials are used to integrate the variation, the fluctuation, and the linearized solution state in each of the primary elements that are members of the reconstruction element. The Lagrange basis functions also provide C^0 continuity along the edges of the reconstruction-elements, thereby ensuring consistent evaluations of the fluctuation through an edge. In this work, the coordinates are always interpolated by linear Lagrange basis functions within a primary element. Along with a high-order interpolation of the solution, this leads to sub-parametric Lagrange-elements.[23] At this stage in the research, the linear interpolation of the coordinates provides some mathematical simplifications and reduces the expense of the numerical integrations. However, this generally requires an assumption of straight edges in the reconstruction elements. For general problems with curved boundaries, higher-order interpolations of the coordinates may be required.

The Lagrange basis functions can be defined in canonical, Fig. 5, or natural, Fig. 6, normalized coordinate systems. The canonical coordinates, ξ and η, are orthogonal while the natural coordinates, L_1, L_2, and L_3,

are related by the expression $L_1 + L_2 + L_3 = 1$. The symmetry of the natural coordinate system allows for application of triangular Gauss quadrature rules.[23] All the integrations required in a primary element are performed using numerical Gauss quadrature. For integration in a specific primary element, a mapping is performed such that the natural coordinate system, typically normalized for the reconstruction element, is instead normalized over the primary element. We define the natural coordinates, normalized over a primary element, as S_1, S_2, and S_3.

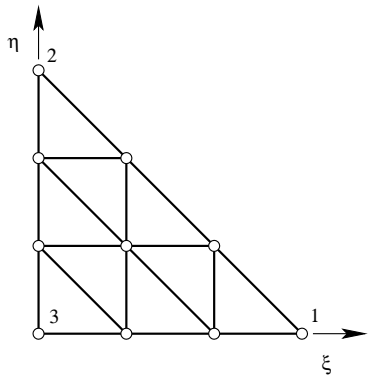

Figure 5. Canonical coordinate system for triangular Lagrange elements.

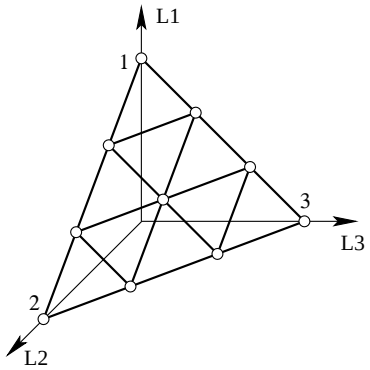

Figure 6. Natural coordinate system for triangular Lagrange elements.

The high-order integration of the linearized state is not necessarily conservative and may not satisfy Eq. 3. To ensure that the scheme is still conservative, a contour-integration-based $\mathcal{RD}$ scheme is used.[24] In this technique, the N scheme (and any derivative schemes) is modified by replacing Eq. 8 with

$$u_{in} = -\frac{\sum_{i=1, i\in E}^{d+1} k_i^+ u_i - \phi^E}{\sum_{i=1, i\in E}^{d+1} k_i^-}. \tag{13}$$

II.C. Boundary Conditions

The asymmetric stencil for the primary elements (the interpolation is not centered about each primary element) allows for a treatment of boundaries that is comparable to approaches used for second-order $\mathcal{RD}$ schemes.

At interior boundaries, interfaces are defined that provide a location to accumulate data from all zones that share a given vertex. As shown in Fig. 7, *edge interfaces* provide connection between zone edges (each vertex is shared by only two zone) and *corner interfaces* provide connection between zone corners (the single vertex can be shared by multiple zones). The residual update from each zone, along with the area contributed to the dual mesh, is accumulated in the interfaces. After updates from all zones sharing an interface are complete, the accumulated data is then redistributed to all the zones. Parallel implementations simply must find a method for accumulating data between separate processes or threads. The only extra requirement for a high-order scheme is to share the order of interpolation along an edge if it may be less than the formal order of the scheme (e.g., an element marked for linear interpolation because of large gradients).

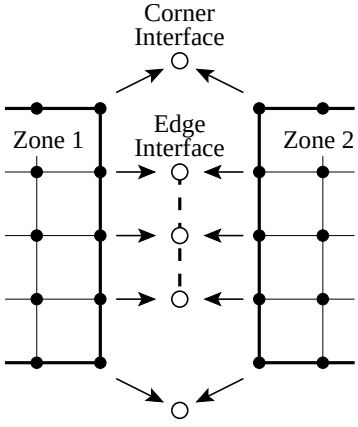

Figure 7. Interfaces defined between two zones for accumulating data.

At domain boundaries, boundary conditions are implemented in "weak" form using a method similar to that proposed by Paillère.[10] In Fig. 8, the elements labelled E1, E2, and E2 are interior elements with vertices V1, V2, and V3 on the domain boundary. Two degenerate ghost elements are assigned to each physical vertex on the domain boundary. In

Fig. 8, the ghost elements GE1 and GE2 are assigned to vertex V2. Since these elements are degenerate, the ghost vertices GV1, GV2, and GV3 are at the exact same position as the physical boundary vertices. This causes the dotted line in Fig. 8 to have zero length and consequently, the contributions to vertices V1 and V3 are zero. Therefore, only vertex V2 is affected by the ghost elements GE1 and GE2. Desired boundary conditions are specified in ghost vertices GV1, GV2, and GV3. The ghost elements are treated the same as physical elements except for the following modifications:

- The linearized state is taken from the value at the physical vertex (vertex 2 for ghost elements GE1 and GE2).
- For the purpose of computing a time step restriction in the ghost element, the area of each ghost element associated with the physical vertex is taken to be half the total physical area of the dual mesh associated with the physical vertex (the contributions made by all the physical elements to the dual mesh at vertex V2 and divided by two).
- The ghost elements are computed with the same local solution-order as the physical element they share an edge with.
- The fluctuation on finite edges of the ghost elements is computed with the aid of one-dimensional Lagrange reconstruction-elements. These one-dimensional Lagrange reconstruction elements follow a particular path depending on which edge is being integrated. Several paths, used for integrating the edges between V2 and V3 (GV2 and GV3), are shown in red, green, and blue in Fig. 8.

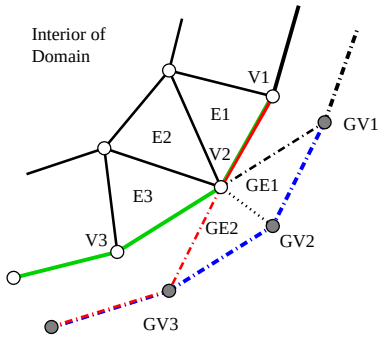

Figure 8. Degenerate ghost cells for defining boundary conditions.

III. An Element Variation Bounded Scheme

Nonlinear stability theory is usually presented in a one-dimensional unsteady framework and constrains the creation, preservation, and destruction of waveforms in the domain. The theory often refers to the total variation (TV) of the solution which is defined by[25]

$$\mathrm{TV}(u) = \sum_i |u(x_{i+1}, t) - u(x_i, t)| \tag{14}$$

for a discrete representation of a function and by

$$\mathrm{TV}(u) = \int \left| \frac{\partial u}{\partial x} \right| \mathrm{d}x \tag{15}$$

for a continuously differentiable function. A scheme is said to be total-variation-diminishing (TVD) if

$$\mathrm{TV}(u^{n+1}) \leq \mathrm{TV}(u^n) \tag{16}$$

and total-variation-bounded (TVB) if

$$\mathrm{TV}(u^n) \leq M \leq \infty \tag{17}$$

for some positive constant M.

The concepts of total-variation-diminishing (TVD) and total-variation-bounded (TVB) reference either the variation at a previous time step or a constant. In this section, these concepts are adapted for steady flows, where temporal evolution of the solution is not a concern. Consequently, the variation of the current solution, based on the high-order interpolant, is instead compared against a trusted reference variation of the solution. This reference is defined to be the variation predicted by a linear interpolation in each element.

The proposed formulation is best presented in one dimension. Figure 9 displays a fourth-order reconstruction element consisting of three primary elements and four degrees of freedom. Also shown is a linear (solid) and cubic (dashed) interpolation of the solution. Of primary interest is the difference in the variation provided by the two interpolations in a primary element, E:

$$\Delta\mathrm{EV}(u) = \mathrm{EV}(u_{k=3}) - \mathrm{EV}(u_{k=1}). \tag{18}$$

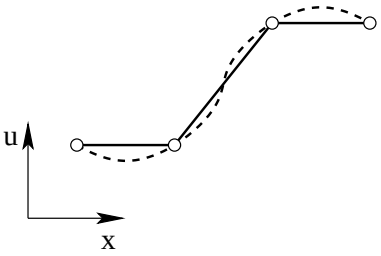

Figure 9. Fourth order reconstruction element consisting of three primary elements in one dimension. A linear (solid) and cubic (dashed) interpolation of the solution is shown.

The notation of element variation (EV) is introduced to define the TV described by Eq. 15 but only integrated over one primary element. It is obvious that $\Delta\mathrm{EV}(u) \geq 0$; the high-order interpolated variation cannot possibly be less than the linearly interpolated variation. When $\Delta\mathrm{EV}(u) = 0$, as in the center element of Fig. 9, the high-order interpolation is satisfactory in the sense that it does not introduce more variation than a linear (and hence monotone) estimation of the variation. When $\Delta\mathrm{EV}(u) > 0$ as in the left and right elements of Fig. 9, the high-order interpolation is increasing the variation and possibly destabilizing the solution. When this is detected, some action should be taken.

If increases in variation are suppressed whenever $\Delta\mathrm{EV}(u) > 0$, the resulting scheme becomes locally analogous to enforcing a TVD condition. If increases in variation are suppressed whenever $\Delta\mathrm{EV}(u) > M$, the resulting scheme becomes locally analogous to enforcing a TVB condition.

III.A. Proposed EVB Scheme

The proposed variation bounded scheme (labeled element-variation-bounded (EVB) scheme) uses a high-order interpolation and LDA distribution scheme wherever possible. The linear interpolation of the variation and a high-order interpolation of the variation are integrated in each element. When

$$\Delta\mathrm{EV}(u) > M\,, \tag{19}$$

the interpolation is reduced to linear in the element E and a blended distribution scheme is used.

It would be preferable to set $M = 0$ and enforce the analogy to the TVD condition. In one dimension, this approach would seem practical since it removes the necessity of defining M. In practice, however, setting $M = 0$ is probably too restrictive. Instead, the value of M tends to define a compromise between damping oscillations near discontinuities and clipping[a] the extrema in smooth regions of flow. For all the solutions in this paper, $M = 0.003$. The motivation for this value will be discussed in more detail later but it is largely based on numerical experiments involving circular advection.

In two-dimensions, the definition of total variation given by Goodman and LeVeque[26] provides a baseline or starting point:

$$\mathrm{TV}(u) = \int |\nabla u|\,\mathrm{d}x\,\mathrm{d}y \quad \text{where} \quad |\nabla u| = \left|\frac{\partial u}{\partial x}\right| + \left|\frac{\partial u}{\partial y}\right|. \tag{20}$$

Unfortunately, it is possible to have $\Delta\mathrm{EV}(u) < 0$ using this definition in two spatial dimensions. Modifications to this definition for application of the EVB approach in multiple dimensions are described below.

III.B. Modifications to the EVB Scheme for Multiple Dimensions

The proposed modifications to the EVB scheme are largely based on observations from numerical experiments. In this section two problems of linear advection are studied. Two profiles, a smooth exponential, $u = \mathrm{e}^{-0.5[(x-0.5)/0.08]^2}$, and a discontinuous "top-hat", are advected at 30° to the grid. Both profiles range

[a]Clipping is an error produced by the TVD condition where the maxima are prevented from increasing and the minima are prevented from decreasing in a smooth solution. Consider a discrete representation of a smooth maximum without a mesh point at the maximum. If the solution shifts such that the maximum is now at a mesh point, the variation will increase. However, this violates the TVD condition and the peak is therefore clipped.

in value from $u = 0$ to $u = 1$. Exact solutions, on a mesh of 48×48 primary elements are shown in Figs. 10 and 11 for the smooth and discontinuous problems, respectively. With a seemingly reasonable

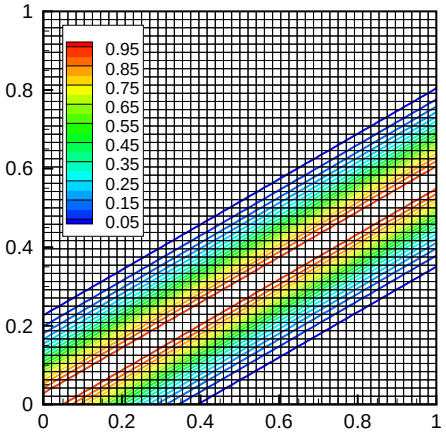

Figure 10. Exact solution to linear advection of a smooth exponential profile on a mesh of 48×48 primary elements.

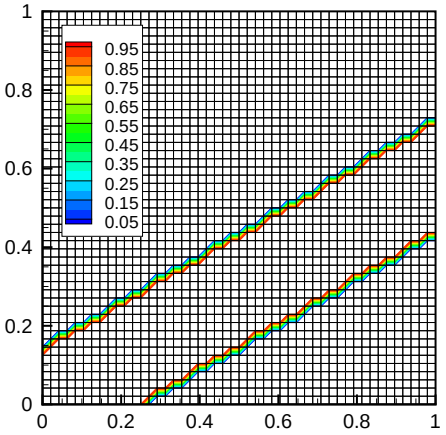

Figure 11. Exact solution to linear advection of a discontinuous "top-hat" profile on a mesh of 48×48 primary elements.

one-dimensional theory and the extension to multiple-dimensions given above, the results from our first numerical experiment were surprising. Figures 12 and 13 show the difference in variation, $\Delta\text{EV}(u)$ (Eqs. 18 and 20), computed with a quadratic interpolation and a cubic interpolation, respectively, for the high-order variation. Both figures illustrate ΔEV computed for an exact representation of the smooth problem on a mesh of 48×48 primary elements. As noted previously, it is expected that in one dimension, ΔEV must be greater than 0. However, both figures show a regular occurrence of elements where $\Delta\text{EV} < 0$.

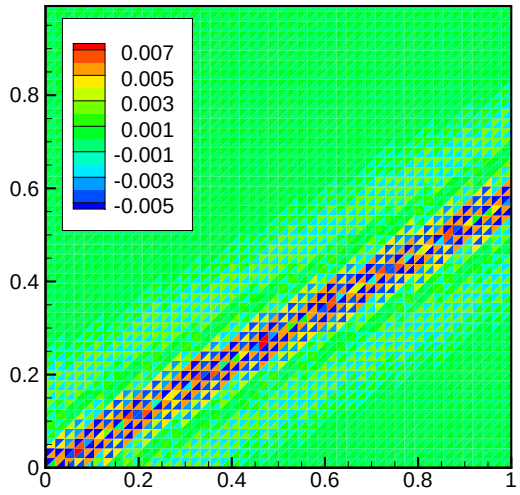

Figure 12. ΔEV computed from a quadratic interpolation of the smooth problem.

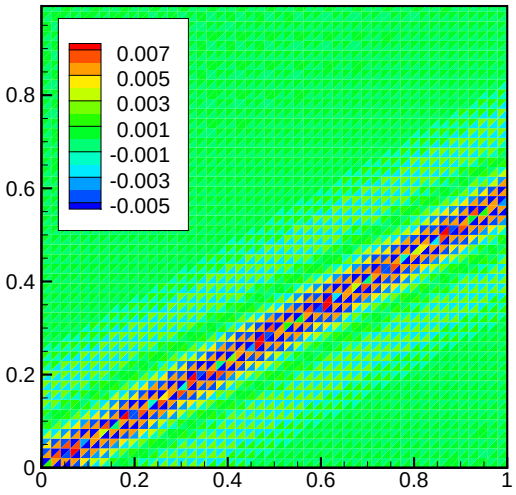

Figure 13. ΔEV computed from a cubic interpolation of the smooth problem.

Interestingly, in each reconstruction element, there is a regular pattern to the ΔEV computed in each primary element. For a quadratic interpolation, the absolute value of the ΔEV is the same for each primary element in a reconstruction element. However, the sign in each element varies as in Fig. 14. Similar behaviour is observed for a cubic interpolation. The signs follow the pattern shown in Fig. 15 but the absolute value is not constant. Instead, it fits the linear interpolant

$$|\Delta\text{EV}| = a\xi + b\eta + c\zeta + d\,, \tag{21}$$

where the canonical coordinates ξ and η correspond to the centroid of each primary element. In the two

sets of elements in Fig. 15, $|\Delta EV|$ can be represented by two planes that are parallel but not coincident. Separation of the planes in Eq. 21 is provided by $\zeta = 1$ for the shaded elements and $\zeta = 0$ otherwise.

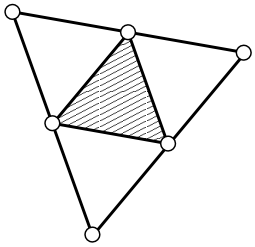

Figure 14. Sign of ΔEV computed in each primary element within a quadratic reconstruction element. The shaded element has opposite sign to the unshaded elements.

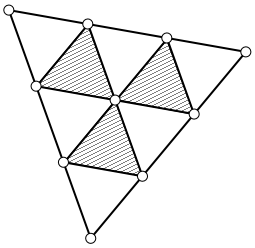

Figure 15. Sign of ΔEV computed in each primary element within a cubic reconstruction element. The shaded elements have opposite sign to the unshaded elements.

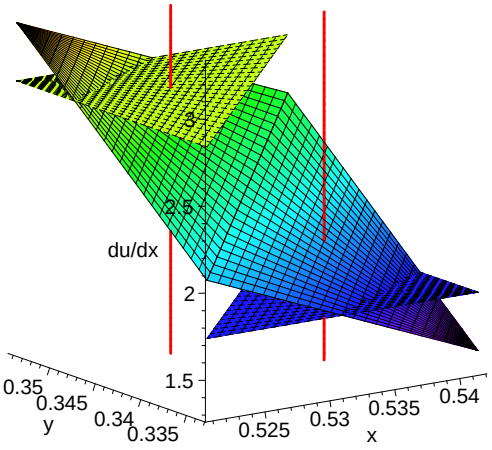

Figure 16. Derivative $\partial u/\partial x$ of the linear and quadratic interpolations of the solution. The centroids of the primary elements are shown by the red lines.

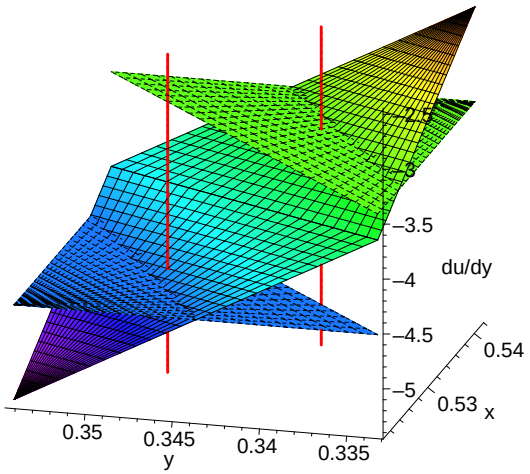

Figure 17. Derivative $\partial u/\partial y$ of the linear and quadratic interpolations of the solution. The centroids of the primary elements are shown by the red lines.

The curious patterns of ΔEV are not fully understood. However, some insight was gained be examining derivatives of the quadratic Lagrange polynomial for a representative reconstruction element. The derivatives $\partial u/\partial x$ and $\partial u/\partial y$ are plotted in Figs. 16 and 17, respectively, for both the linear and quadratic interpolations. Two primary elements are shown in each of these figures, one with positive ΔEV and one with negative ΔEV, as illustrated in Fig. 18. As expected, the linear derivatives have constant value while the quadratic derivative is represented by a plane. The centroids of the primary elements are shown by the red lines (marking a sampling location for Gauss quadrature of the derivatives). In both cases, one primary element has one linear derivative greater than the quadratic derivative, and one linear derivative less than the quadratic derivative. A one-dimensional interpretation of the positive and negative variation is shown in Fig 19. Two primary elements are shown in a quadratic reconstruction element. Again, the linear derivatives are constant and the quadratic derivative is represented by a sloped line. Although the average derivative, from both interpolations, is of the same value in the reconstruction element, positive and negative ΔEV is shown. In one space dimension, it is not possible to obtain the derivatives shown in Fig 19 and have the linear and quadratic interpolations match at the vertices. However, it appears that in multiple dimensions, extra degrees of freedom are available that permit this behaviour.

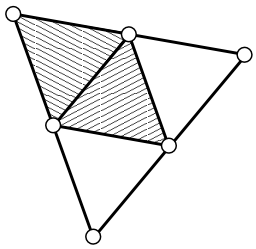

Figure 18. Primary elements in a reconstruction element that are plotted in Figs. 16 and 17.

With this understanding, a simple technique was devised to cancel out the positive and negative patterns of ΔEV within a reconstruction element. Using least squares, a constant value for quadratic interpolation and Eq. 21 for cubic interpolation is fit to $|\Delta EV|$ in each reconstruction element. Next, a correlation is developed between the shaded and unshaded subgroups of primary elements in either Fig. 14 or 15 and the fit. The subgroup with the largest correlation with the fit contains the positive elements. Finally, the fit is either added or subtracted from the ΔEV in each primary element, depending on the sign in the element.

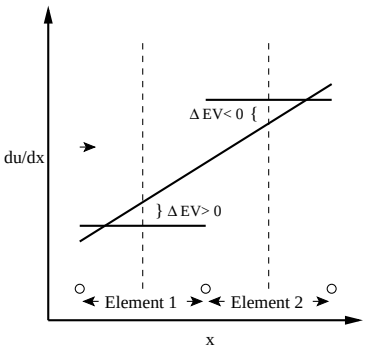

Figure 19. A one-dimensional representation of the positive and negative ΔEV observed in two dimensions.

It should be mentioned that the regular pattern which allows for the cancellation is a bit fortuitous in Figs 12 and 13. It is dependent on the alignment of the element edges with the coordinate directions. This, and the fact that the definition of the variation given by Eq. 20 is dependent upon the orientation of the coordinate system, can be corrected by instead computing the variation as a function of the natural coordinates in the Lagrange element. The derivatives $\partial u/\partial x$ and $\partial u/\partial y$ are obtained as follows. Defining the natural coordinates in a primary element to be S_1, S_2, and S_3 one can obtain

$$\frac{\partial \phi}{\partial S_1}, \quad \frac{\partial \phi}{\partial S_2}, \quad \text{and} \quad \frac{\partial \phi}{\partial S_2} \tag{22}$$

from the Lagrange polynomial where ϕ is either u, x, or y. A switch to the canonical coordinates, $\xi = S_1$, $\eta = S_2$, and $1 - \xi - \eta = S_3$ is made by

$$\begin{aligned} \frac{\partial \phi}{\partial \xi} &= \frac{\partial \phi}{\partial S_1}\frac{\partial S_1}{\partial \xi} + \frac{\partial \phi}{\partial S_2}\frac{\partial S_2}{\partial \xi} + \frac{\partial \phi}{\partial S_3}\frac{\partial S_3}{\partial \xi} \\ &= \frac{\partial \phi}{\partial S_1} - \frac{\partial \phi}{\partial S_3}\,, \\ \frac{\partial \phi}{\partial \eta} &= \frac{\partial \phi}{\partial S_1}\frac{\partial S_1}{\partial \eta} + \frac{\partial \phi}{\partial S_2}\frac{\partial S_2}{\partial \eta} + \frac{\partial \phi}{\partial S_3}\frac{\partial S_3}{\partial \eta} \\ &= \frac{\partial \phi}{\partial S_2} - \frac{\partial \phi}{\partial S_3}\,. \end{aligned} \tag{23}$$

The coordinate Jacobian is defined by

$$\mathbf{J} = \begin{bmatrix} \frac{\partial x}{\partial \xi} & \frac{\partial y}{\partial \xi} \\ \frac{\partial x}{\partial \eta} & \frac{\partial y}{\partial \eta} \end{bmatrix} \tag{24}$$

and the derivatives $\partial u/\partial x$ and $\partial u/\partial y$ are computed as

$$\begin{bmatrix} \frac{\partial u}{\partial x} \\ \frac{\partial u}{\partial y} \end{bmatrix} = \mathbf{J}^{-1} \begin{bmatrix} \frac{\partial u}{\partial \xi} \\ \frac{\partial u}{\partial \eta} \end{bmatrix}\,. \tag{25}$$

To express the derivatives with the symmetry of the natural coordinate system, start from Eq.23 but also with

$$\frac{\partial u}{\partial \zeta} \equiv \frac{\partial u}{\partial S_1} - \frac{\partial u}{\partial S_2} \tag{26}$$

In place of Eq. 20, the element variation is defined as

$$\mathrm{EV} = \left|\frac{\partial u}{\partial \xi}\right| + \left|\frac{\partial u}{\partial \eta}\right| + \left|\frac{\partial u}{\partial \zeta}\right|. \tag{27}$$

The meaning of the derivatives used to compute the variation is not entirely clear. It is known that one cannot simply use $\partial u/\partial S_1$, $\partial u/\partial S_2$, and $\partial u/\partial S_3$ since the natural coordinates in the plane are not orthogonal. Also, Eq. 26 would have been derived had one chosen the relationship between the canonical and natural coordinates to be $\xi = S_1$, $\eta = S_3$, and $1 - \xi - \eta = S_2$. Equation 27 obviates the freedom in choosing the relationship between the canonical and natural coordinates by incorporating all the differences

$$\frac{\partial u}{\partial S_i} - \frac{\partial u}{\partial S_j}, \quad i = 1, 2, 3, \quad j = (i \bmod 3) + 1\,. \tag{28}$$

Note that Gauss quadrature of Eq. 27 may not be exact because the absolute value of the derivative could change discontinuously near extrema in the solution. To circumvent this issue, a larger number of Gauss points were used in the integration. In practice, however, using the extra Gauss points did not make much difference indicating that this issue may not be of much concern.

Contour plots are now shown of ΔEV computed from the cubic and linear interpolations of exact solutions to the two profiles shown in Figs. 10 and 11. Equation 27 is used to integrate the variation and results are shown with and without cancellation of the positive and negative ΔEV within a reconstruction-element. Figure 20 displays the ΔEV computed in each primary element for the exact solution to the smooth problem. The cancellation tends to focus the non-zero ΔEV on the maximum in the center of the exponential profile. At a mesh size of 96×96 primary elements, the maximum is clearly identifiable. At mesh size 192×192, ΔEV falls below visible levels demonstrating that local extrema in smooth solution will not be detected with sufficient mesh refinement. Figure 21 displays the ΔEV computed in each primary element for the exact solution to the discontinuous problem. The effect of the cancellation is to set ΔEV in some elements closer to zero. However, in all cases, the discontinuity is well represented by tight bands where $|\Delta\text{EV}| > 0$. The magnitude of the variation does not vary with mesh size indicating that integration of the variation properly scales with mesh size. Therefore, the discontinuities will still be detected with mesh refinement. That extrema in smooth solutions are not captured at fine mesh levels while there is virtually no effect on discontinuities indicates that adaptive mesh refinement would be a useful tool for isolating discontinuities.

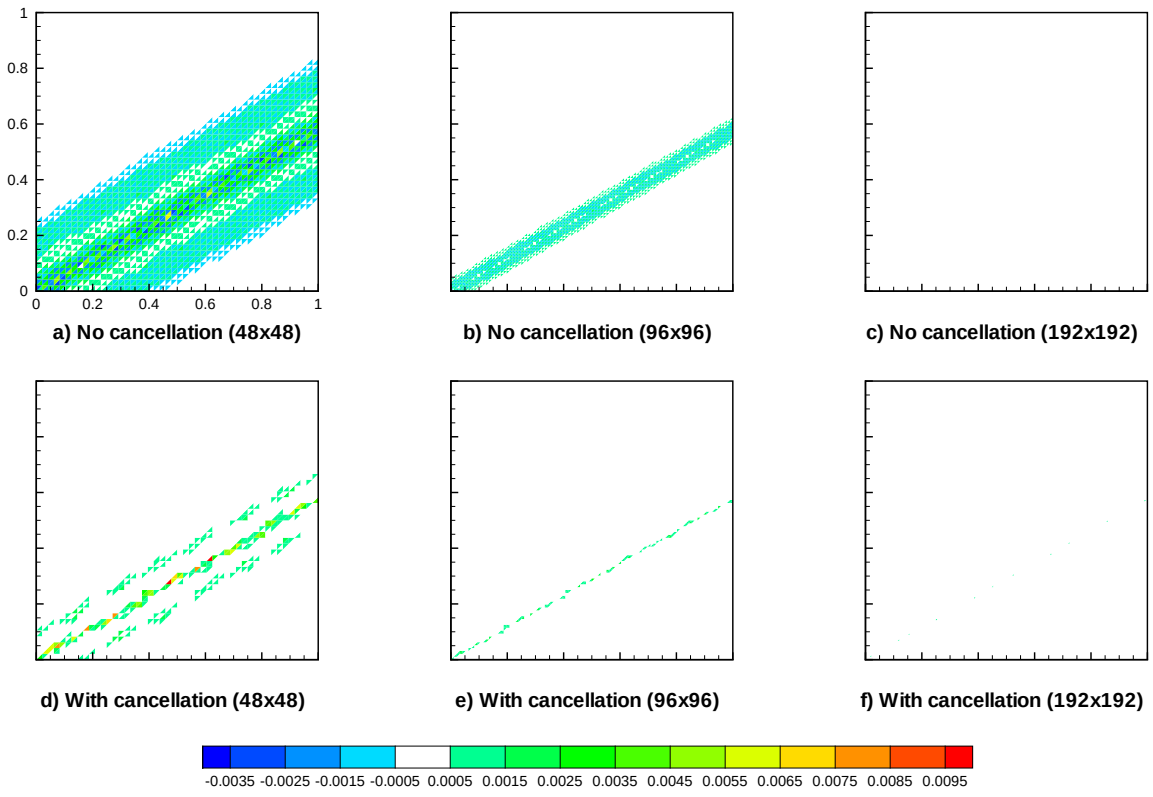

Figure 20. Computed values of ΔEV from the exact solution to the smooth advection problem for various mesh sizes. Results are shown with and without cancellation of the positive and negative ΔEV within a reconstruction element.

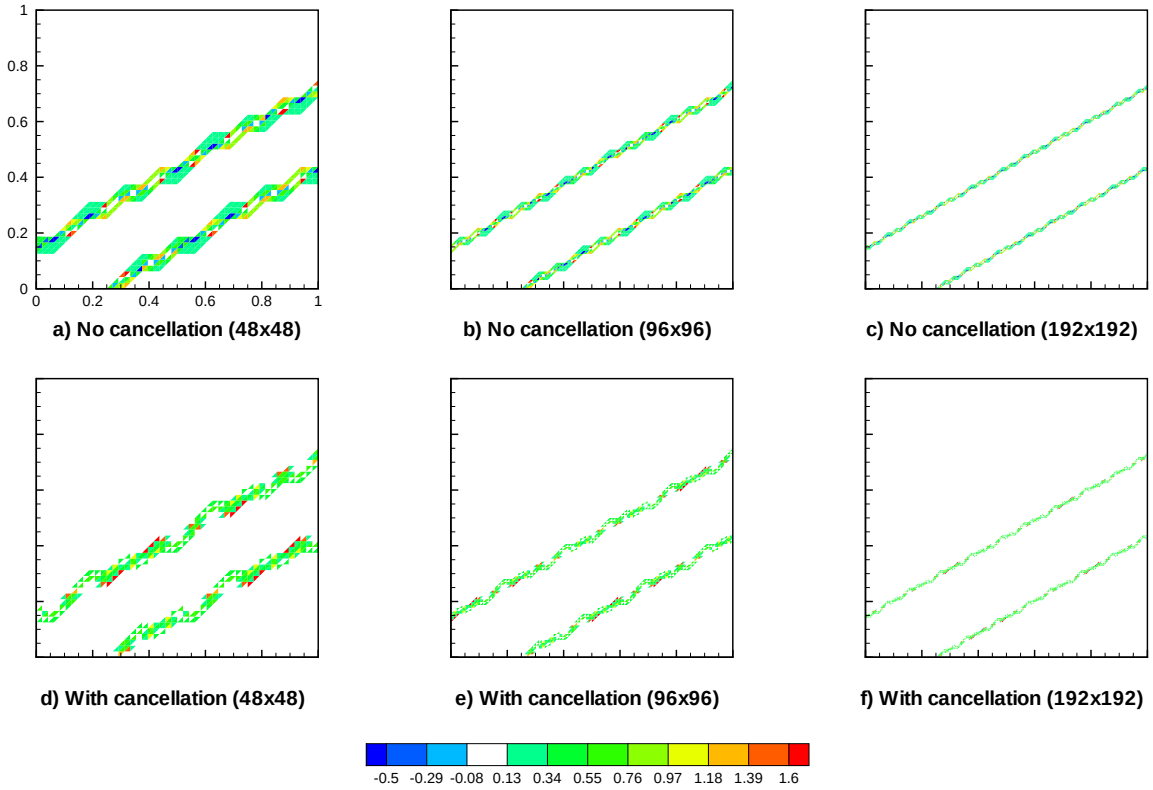

Figure 21. Computed values of ΔEV from the exact solution to the discontinuous advection problem for various mesh sizes. Results are shown with and without cancellation of the positive and negative ΔEV within a reconstruction element.

IV. Numerical Method

Although the EVB $\mathcal{RD}$ scheme can be implemented on an unstructured mesh of reconstruction elements, in this work quadrilateral meshes are used for the numerical computations. Since $\mathcal{RD}$ solutions are computed on simplexes (triangles), the freedom exists to optimally tessellate each quadrilateral by inserting a diagonal that is aligned with the advection vector. The reconstruction elements are constructed in a similar manner. For a fourth-order solution, a 3×3 collection of quadrilaterals is grouped together. This collection is divided into two reconstruction elements by inserting a diagonal aligned with the average advection vector over the 16 vertices in the collection. The concept is illustrated in Fig. 22. Note that the tessellation of the primary elements may be restricted by the tessellation of the reconstruction element.

The following steps summarize the numerical method used to obtain the fourth-order results presented in the next section.

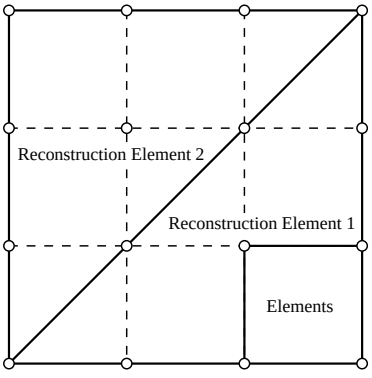

Figure 22. Creation of cubic reconstruction-elements from a 3×3 collection of quadrilaterals

1. A cubic-reconstruction and blended $\mathcal{RD}$ scheme is iterated using explicit-Euler time-marching until the solution is satisfactorily developed.

2. The ΔEV is computed in each primary element and compared against a cut-off value $M = 0.003$. If ΔEV is greater than M, the element is marked as requiring a linear interpolation. The blended distribution scheme is used in second-order elements and the LDA distribution scheme in high-order elements. The tessellation of the reconstruction elements is frozen.

3. After a few hundred iterations. The blending coefficient is frozen for primary elements that use the

blended scheme. The tessellation of the primary elements is also frozen. The residuals are converged as desired; in this work, the residuals are converged by at least ten orders of magnitude.

V. Numerical Results

A formal proof that the proposed EVB scheme does indeed bound the variation according to the definition of TVB in multiple dimensions is beyond the scope of this work. Instead, numerical experiments are used to demonstrate the expected behaviour, namely:

- the strength of the nonlinear stability condition can be sufficiently weakened to eliminate undesirable behaviour such as clipping in smooth solutions.
- the nonlinear stability condition should satisfactorily dampen numerical oscillations near discontinuities.

The behaviours listed above are related. A scheme that eliminates all oscillations will typically clip. A scheme the does not clip must permit some oscillation. The challenge is finding a suitable (and problem-independent) compromise.

The performance of the EVB scheme is examined for solutions to the non-linear Burgers equation and to linear problems of circular advection.

V.A. Non-Linear Burgers Equation

The exact solution to the non-linear Burgers equation, given by

$$\frac{\partial u}{\partial t} + u\frac{\partial u}{\partial x} + 1\frac{\partial u}{\partial y} = 0\,, \tag{29}$$

is displayed in Fig. 23. Along the x-axis, the solution u is varied linearly from 1.5 to -0.5. This results in a compression wave that strengthens and produces a shock at $(x = 0.75, y = 0.5)$. The ability of the EVB scheme to detect the shock is illustrated in Fig. 24. Elements that have been marked as requiring a linear interpolation are colored black. The shock is correctly detected by the EVB scheme and marking of the elements seems to be independent of the mesh size. The discontinuous change of the solution at the leading and trailing edges of the compression wave is also marked. However, this marking is only prevalent on the coarser meshes and the edges of the compression wave tend to be ignored as the mesh is refined.

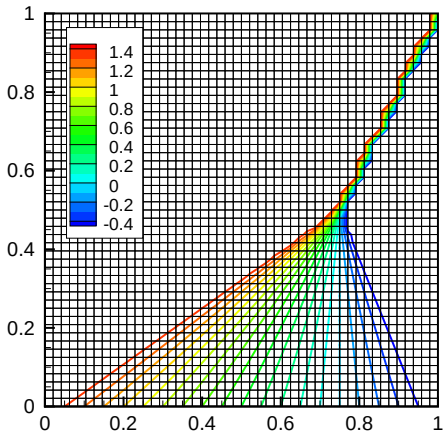

Figure 23. Exact solution to Burgers equation, represented on a mesh of 48×48 primary elements.

The effectiveness of the EVB scheme at enforcing monotonicity is illustrated in Fig. 25. A cross-section of the shock is plotted at $y = 0.708334$. The second-order LN (MUSCL) and blended schemes perform equally well at preserving monotonicity. Interestingly, the fourth-order blended scheme creates some overshoots that nearly match the magnitude of the overshoots in the fourth-order LDA scheme. This indicates the

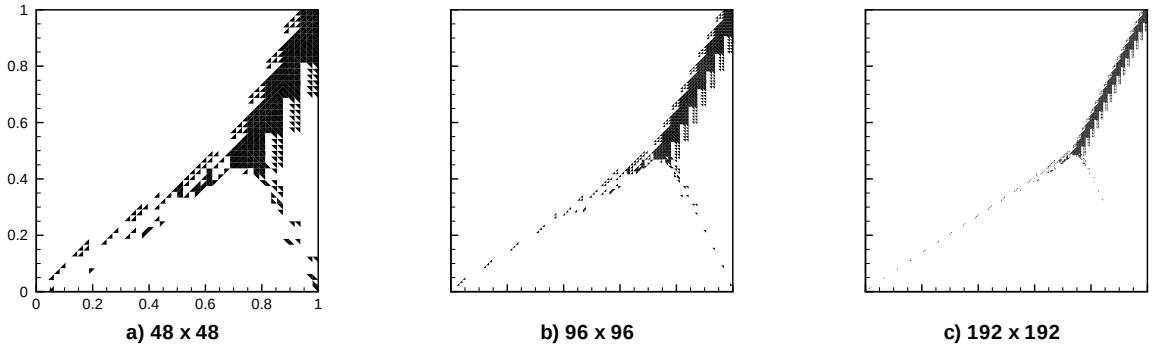

Figure 24. Primary elements marked for a linear interpolation by the EVB scheme for Burgers equation. The shock is similarly marked for all mesh sizes.

importance of reducing the order of the interpolation to linear in the vicinity of discontinuities. The EVB scheme indicates monotonicity on par with the second-order scheme. Oscillations over the entire domain are plotted in Fig. 26. The results generally agree with the profile in Fig. 25. The accuracy of each solution

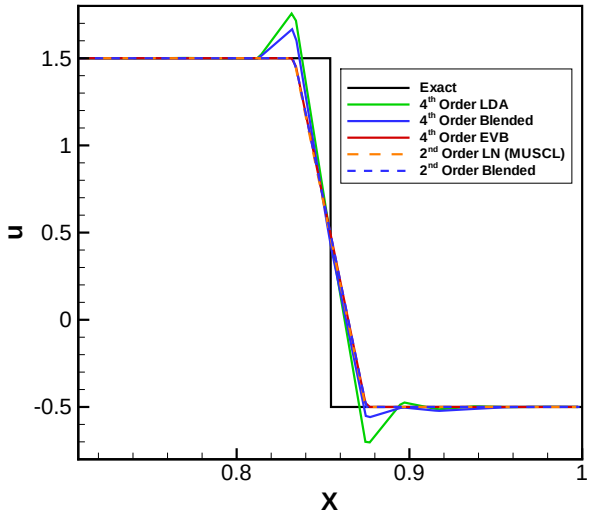

Figure 25. Cross-section of solutions to Burgers equation on a mesh of size 48×48. The cross-section is taken at $y = 0.708334$.

as a function of mesh density per dimension is shown in Fig. 27. Because of the discontinuity, all schemes have a spatial order-of-convergence less than one. Although not of much significance (monotonicity is more important for this problem), the EVB scheme provides the lowest solution error.

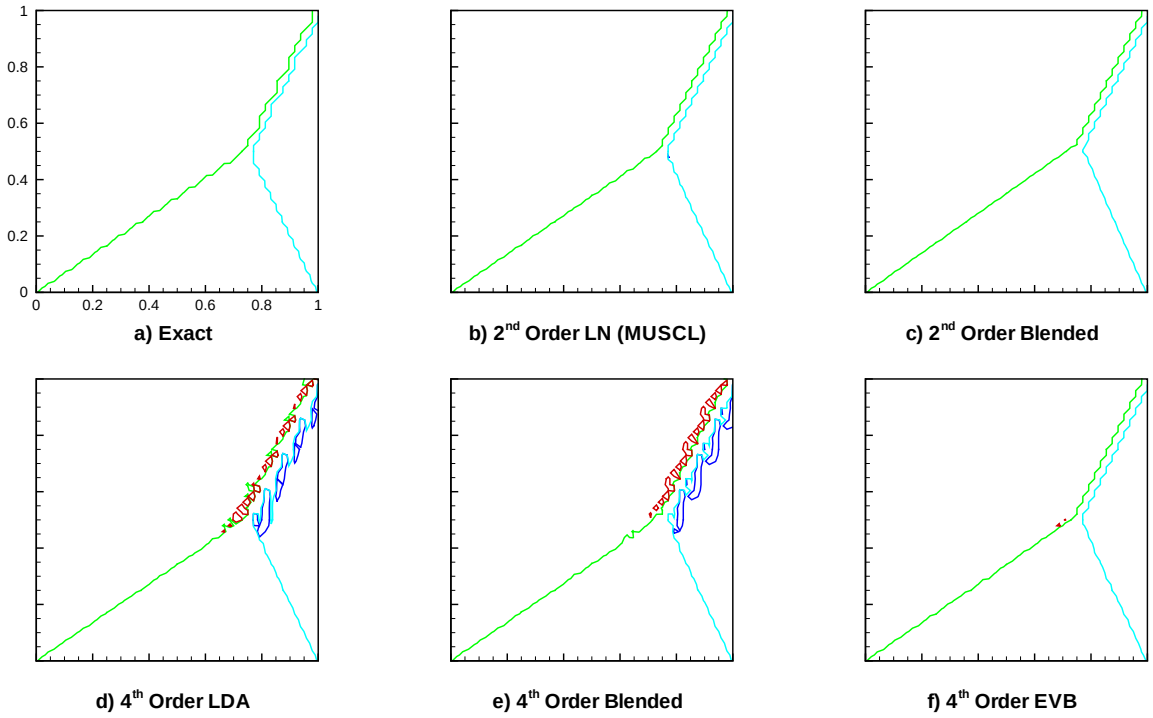

Figure 26. Oscillations in solutions to Burgers equation on a mesh of size 48×48. Contour levels: blue -0.51, cyan -0.49, green 1.49, red 1.51.

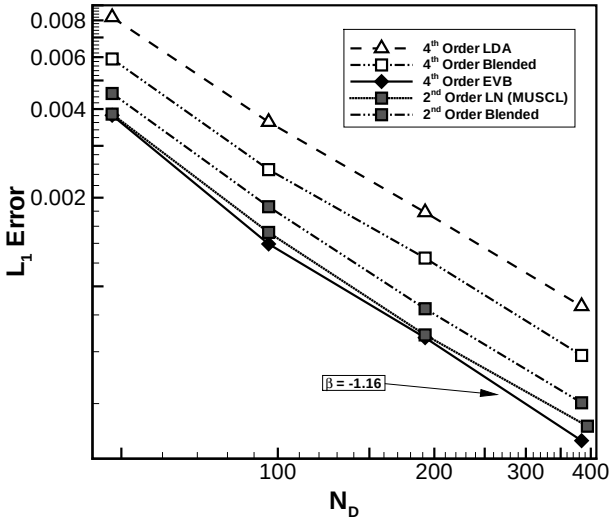

Figure 27. Spatial accuracy for solutions to Burgers equation.

V.B. Linear Circular Advection

The performance of the EVB scheme was also examined for the problem of linear circular advection. The linear advection equation is given by

$$\frac{\partial u}{\partial t} + a\frac{\partial u}{\partial x} + b\frac{\partial u}{\partial y} = 0\,, \tag{30}$$

where $a = a(x, y)$ and $b = b(x, y)$ are the components of the advection velocity field. The two advected profiles considered here, a smooth exponential and a discontinuous "top-hat", are the same as previously described in section III.B. Exact solutions and meshes of size 48×48 are shown in Figs. 28 and 29. The inflow/outflow

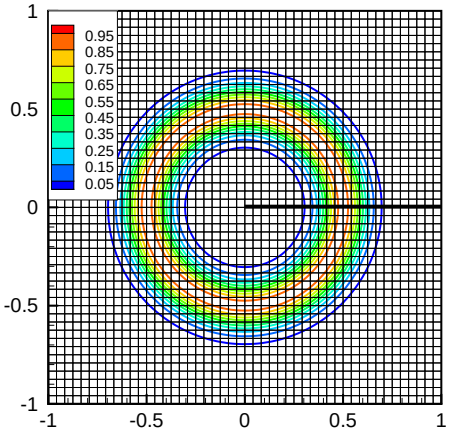

Figure 28. Exact solution to circular advection of a smooth exponential profile and a mesh of 48×48 primary elements.

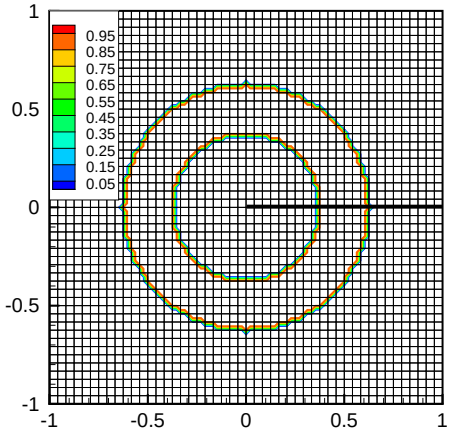

Figure 29. Exact solution to circular advection of a discontinuous "top-hat" profile and a mesh of 48×48 primary elements.

boundary extends along $(0 \le x \le 1, y = 0)$ as shown by the thick black line in the figures. The initial profile is assigned at this boundary and then advected $360\,^\circ$ in a counter-clockwise direction.

In Fig. 30, elements that have been marked as second-order are shaded black. Plots are shown for the smooth and discontinuous problems solved on meshes of size 96×96, 192×192, and 384×384. As with previous results, the discontinuity is captured well, irrespective of the mesh size, while the maximum in the smooth profile is not detected on the finest mesh. Although perhaps not visible, three elements near the outflow boundary are still marked as second-order in Fig. 30c.

The effectiveness of the various schemes at damping oscillations is illustrated in Fig. 31 for solutions involving the discontinuous profile. This figure displays a cross-section of the solution on the 96×96 mesh after advecting $180\,^\circ$. Similar to Fig. 25, the second-order LN (MUSCL) and blended solutions are monotone. While the fourth-order LDA scheme exhibits large overshoots, the fourth-order blended scheme does quite well; the only observable overshoot is at $x = -0.31$. The EVB scheme performs similarly to the second-order blended scheme. Oscillations over the entire domain are plotted in Fig. 32. The results were again computed on a 96×96 mesh. It can be seen that oscillations are present in the fourth-order blended scheme but they disappear quickly as the solution gradients dissipate. Interestingly, the second-order LN scheme with a MUSCL limiter generates the result that most closely approximates the exact solution.

The spatial order of accuracy is illustrated in Fig. 33 for the smooth problem and Fig. 34 for the discontinuous problem. In Fig. 33, the EVB scheme initially has the worst accuracy but approaches the accuracy of the fourth-order LDA scheme as the increasing mesh density reduces the number of elements with a linear interpolation. However, even with only three elements marked for a linear interpolation on the finest mesh, the EVB scheme still has an absolute error almost an order of magnitude greater than the fourth-order LDA scheme. The behaviour of the fourth-order blended scheme is unexpected in this figure, having a convergence rate much less than four. In Fig. 34, the discontinuity causes all solutions to have a spatial order of convergence less than one. Interestingly, the fourth-order LDA scheme is the most accurate, perhaps because the gradients in the discontinuity dissipate quite rapidly.

Figure 35 attempts to illustrate the benefits, in terms of computation time, from using a high-order algorithm on smooth problems. This figure was generated from the results for circular advection of the smooth

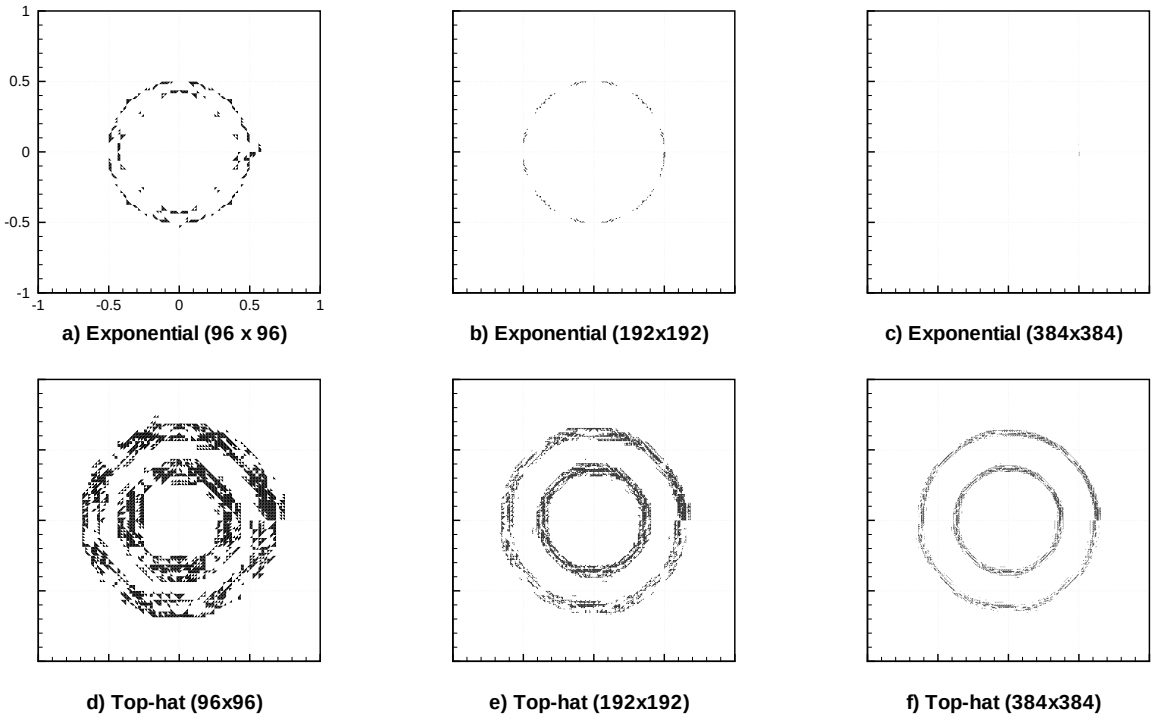

Figure 30. Elements in which the interpolation order is reduced to linear by the EVB scheme.

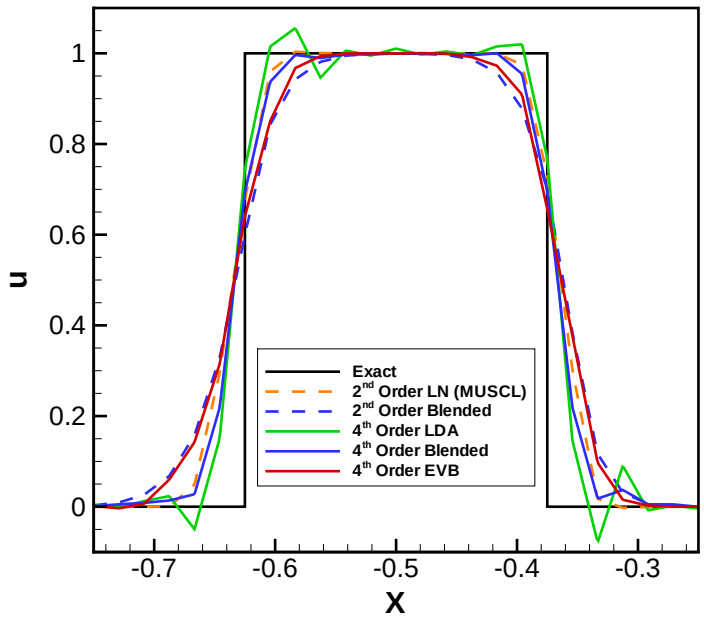

Figure 31. Cross-section of solutions to circular advection of the discontinuous profile. The mesh size is 96×96 and the cross-section is taken after advecting 180°.

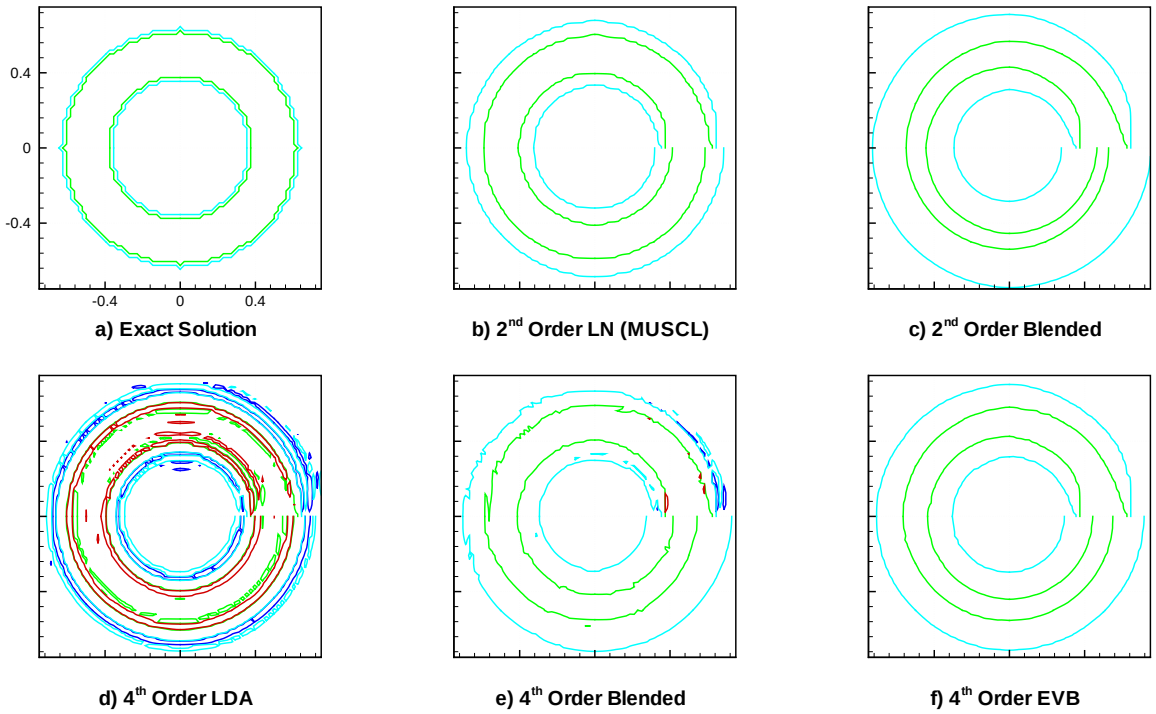

Figure 32. Oscillations in solutions to circular advection of the discontinuous profile on a mesh of size 96×96. Contour levels: blue -0.01, cyan -0.01, green 0.99, red 1.01.

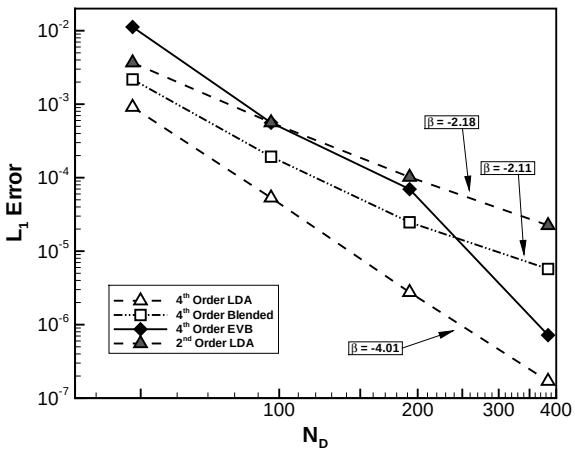

Figure 33. Spatial accuracy for advection of the smooth profile.

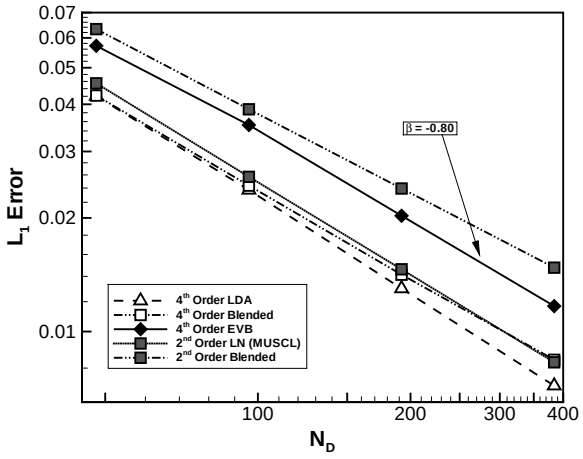

Figure 34. Spatial accuracy for advection of the discontinuous profile.

profile and all computation times have been normalized by the time for computing a second-order solution on the coarsest mesh. The fourth-order LDA scheme drastically outperforms anything else, quickly having a computation time that is orders of magnitude lower than the second-order schemes for a comparable level of accuracy. The EVB scheme, on the other hand, performs rather poorly. In general, it only outperforms the second-order blended scheme except on the finest mesh. The importance of eliminating clipping on coarser mesh densities is obvious as the EVB scheme will not approach the fourth-order LDA scheme until all elements use a fourth-order interpolation. As implemented, the fourth-order schemes have a computation time approximately three times that of the second-order schemes for the same mesh.

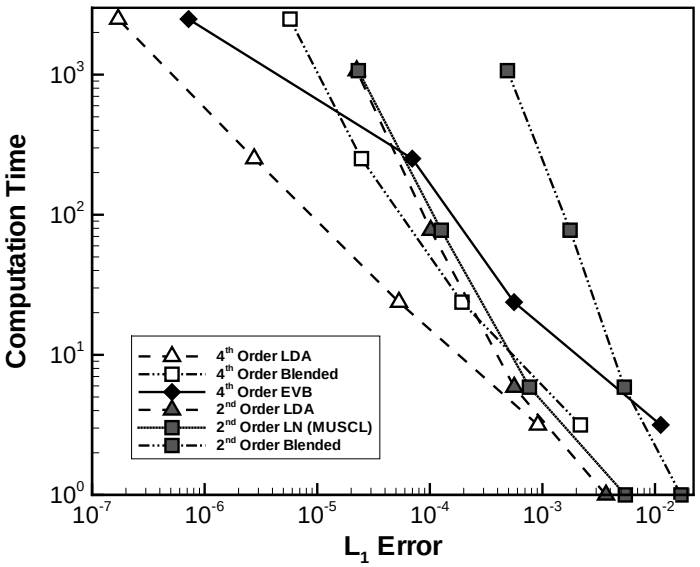

Figure 35. Computation time required for a given accuracy for solutions to circular advection of the smooth profile.

V.C. Comments on the Results

As noted previously, the cut-off value M for marking an element as second-order was set to 0.003. This value was selected based on numerical experiments involving problems of circular advection with the goal of finding the largest value that would still satisfactorily dampen oscillations in the solution. In some sense, the EVB method is disappointing because, even on very fine meshes, some elements are still marked as second-order in the smooth solution (see Fig. 30c). Although there is always a trade-off between damping oscillations and clipping smooth extrema, we had hoped for less compromise on the finer meshes. If the EVB method would not mark smooth extrema on more moderate meshes, then mesh refinement could be used more effectively to eliminate clipping. A couple of reasons have been identified for the poor performance of the EVB method when applied to problems of circular advection:

1. The discontinuity in the circular advection problem is a contact surface and therefore more prone to numerical dissipation (as opposed to a shock in which the converging characteristics tend to counter the numerical dissipation). Consequently, the gradients tend to diminish and the EVB scheme detects smooth undulating waves rather than sharp overshoots. Although perhaps tolerable in practice, these waves were damped in this work such that the Figs. 31 and 32 would be more or less non-oscillatory. This may have required setting M too large.

2. Since the interpolation for a primary element is not necessarily centered, local extrema in the solution can exist between the reconstruction elements. Consider the diagonal inserted into the collection of quadrilateral elements in Fig. 22. A local maximum in the solution could exist along this line and not be detected by computations of ΔEV in the reconstruction elements on either side of the line. Both reconstruction elements would simply detect a monotonically increasing solution towards the line. This behaviour has been observed in circular advection solutions of the discontinuous profile. Since ΔEV is only computed once in a simulation, and is therefore relatively inexpensive to compute, it would be prudent to test for extrema between the reconstruction elements. This may help detect extrema and allow for a lower value of M.

3. In the solution to circular advection of a smooth profile on the finest mesh (384×384), only three elements were marked as second order. All these elements are near the outflow boundary and seem to have a value about twice that at other symmetrical locations in the flow. The large values of ΔEV may be the result of interaction with the outflow boundary. Had those three elements not been marked as second order, no clipping would have occurred and the solution would be identical to that produced by

the LDA scheme. Consequently, the results shown may have been undesirably influenced by boundary conditions.

As a final note, although the solution range for problems involving Burgers equation was twice that of the circular advection problems ($-0.5 \rightarrow 1.5$ vs. $0 \rightarrow 1$), the same cut-off value of $M = 0.003$ was used. A more tuned selection of M might alleviate the marking of second-order elements at the leading and trailing edges of the compression fan in the solution to Burgers equation. The scaling of M, such that it is representative for all problems, has not yet been investigated.

VI. Conclusion

A high-order $\mathcal{RD}$ scheme has been developed that controls solution monotonicity in the vicinity of discontinuities by implementing an analogue of TVB. The proposed EVB scheme compares the variation between high-order and linear interpolations of the solution within an element to detect unresolved gradients. Elements with unresolved gradients are solved using a linear interpolation and a blended distribution scheme. All other elements are solved with a high-order interpolation and an LDA distribution scheme.

Numerical experiments indicate the necessity of reducing a high-order interpolation to linear in the vicinity of discontinuities. It is not sufficient to simply use a positive distribution scheme. It is shown in the results that the EVB scheme can effectively identify unresolved gradients and suppress oscillations near discontinuities in a manner comparable to second-order positive $\mathcal{RD}$ schemes. Moreover, the detection and damping of oscillations is consistent for all mesh resolutions.

Unfortunately, the high-order EVB scheme is also quite aggressive at clipping the extrema of smooth solutions. While the scheme tends to ignore smooth extrema as the mesh is refined, the results indicate that very fine meshes are required to eliminate the clipping entirely. Several reasons were given as to why the clipping of the EVB scheme persists on such fine meshes and these provide an avenue for possible improvements to the proposed scheme. The goal of using the EVB scheme to increase solution accuracy in smooth regions is considered unfulfilled until clipping can be eliminated on more moderate mesh sizes.

Finally, it was shown that the high-order methods can drastically reduce the computation time compared to second order methods. An improved EVB scheme, coupled with mesh refinement, could prove to be an effective method for reducing the computational cost of simulations that feature both detailed smooth flows and discontinuities.

VII. Acknowledgments

The first author would like to thank Xinfeng Gao for the many interesting discussions on the topic of multi-dimensional variation.

References

[1]Roe, P. L. and Sidilkover, D., "Optimum Positive Linear Schemes for Advection in Two and Three Dimensions," *SIAM Journal of Numerical Analysis*, Vol. 29, No. 6, December 1992, pp. 1542–1568.

[2]Deconinck, H., Sermeus, K., and Abgrall, R., "Status of Multidimensional Upwind Residual Distribution Schemes and Applications in Aeronautics," AIAA 2000-2328, AIAA Fluids Conference, 2000.

[3]Abgrall, R., "Toward the Ultimate Conservative Scheme: Following the Quest," *Journal of Computational Physics*, Vol. 167, 2001, pp. 277–315.

[4]Wood, W. A. and Kleb, W. L., "2-D/Axisymmetric Formulation of Multi-dimensional Upwind Scheme," AIAA 2001-2630, 15th AIAA CFD Conference, 2001.

[5]Guzik, S. M. J. and Groth, C. P. T., "Comparison of Solution Accuracy of Multidimensional Residual Distribution and Godunov-Type Finite-Volume Methods," *International Journal of Computational Fluid Dynamics*, 2008, Accepted for publication.

[6]Abgrall, R., "Construction of Second Order Accurate Monotone and Stable Residual Distribution Schemes for Unsteady Flow Problems," *Journal of Computational Physics*, Vol. 168, 2003, pp. 16–55.

[7]Ricchiuto, M., Csík, A., and Deconinck, H., "Residual Distribution for General Time-Dependent Conservation Laws," *Journal of Computational Physics*, Vol. 209, 2005, pp. 249–289.

[8]van Leer, B., "Towards the Ultimate Conservative Difference Scheme. V. A Second-Order Sequel to Godunov's Method," *Journal of Computational Physics*, Vol. 32, 1979, pp. 101–136.

[9]Deconinck, H., Powell, K. G., Roe, P. L., and Struijs, R., "Multi-Dimensional Schemes for Scalar Advection," AIAA 91-1532, AIAA CFD Conference, 1991.

[10]Paillère, H., *Multidimensional Upwind Residual Distribution Schemes for the Euler and Navier-Stokes Equations on Unstructured Grids*, Ph.D. thesis, Université Libre de Bruxelles, June 1995.

[11]Struijs, R., *A Multi-Dimensional Upwind Discretization Method for the Euler Equations on Unstructured Grids*, Ph.D. thesis, Technische Universiteit Delft, June 1994.

[12]Sidilkover, D. and Roe, P. L., "Unification of some Advection Schemes in Two Dimensions," Technical Report 95-10, ICASE, 1995.

[13]Waterson, N. P. and Deconinck, H., "Design Principles for Bounded Higher-Order Convection Schemes — a Unified Approach," *Journal of Computational Physics*, Vol. 224, 2007, pp. 182–207.

[14]Mesaros, L. M., *Multi-Dimensional Fluctuation Splitting Schemes for the Euler Equations on Unstructured Grids*, Ph.D. thesis, University of Michigan, 1995.

[15]Rad, M., *A Residual Distribution Approach to the Euler Equations that Preserves Potential Flow*, Ph.D. thesis, University of Michigan, 2001.

[16]van der Weide, E., Deconinck, H., Issman, E., and Degrez, G., "A Parallel, Implicit, Multi-Dimensional Upwind, Residual Distribution Method for the Navier-Stokes Equations on Unstructured Grids," *Computational Mechanics*, Vol. 23, 1999, pp. 199–208.

[17]Abgrall, R. and Roe, P. L., "High Order Fluctuation Schemes on Triangular Meshes," *Journal of Scientific Computing*, Vol. 19, No. 1-3, December 2003, pp. 3–36.

[18]Abgrall, R. and Mezine, M., "Construction of Second-Order Accurate Monotone and Stable Residual Distribution Schemes for Steady Problems," *Journal of Computational Physics*, Vol. 195, 2004, pp. 474–507.

[19]Abgrall, R., "Essentially Non-Oscillatory Residual Distribution Schemes for Hyperbolic Problems," *Journal of Computational Physics*, Vol. 214, 2006, pp. 773–808.

[20]Caraeni, D. and Fuchs, L., "Compact Third-Order Multidimensional Upwind Discretization for Steady and Unsteady Flow Simulations," *Computers & Fluids*, Vol. 34, 2005, pp. 419–441.

[21]Hubbard, M. E. and Laird, A. L., "Achieving High-Order Fluctuation Splitting Schemes by Extending the Stencil," *Computers & Fluids*, Vol. 34, 2005, pp. 443–459.

[22]Chou, C.-S. and Shu, C.-W., "High Order Residual Distribution Conservative Finite Difference WENO Schemes for Convection-Diffusion Steady State Problems on Non-Smooth Meshes," *Journal of Computational Physics*, Vol. 224, 2007, pp. 992–1020.

[23]Zienkiewicz, O. C., *Finite Element Method in Engineering Science*, McGraw-Hill Education, 2nd ed., 1972.

[24]Csík, A., Ricchiuto, M., and Deconinck, H., "A Conservative Formulation of the Multidimensional Upwind Residual Distribution Schemes for General Nonlinear Conservation Laws," *Journal of Computational Physics*, Vol. 179, 2002, pp. 286–312.

[25]Harten, A., "High Resolution Schemes for Hyperbolic Conservation Laws," *Journal of Computational Physics*, Vol. 49, 1983, pp. 357–393.

[26]Goodman, J. B. and LeVeque, R. J., "On the Accuracy of Stable Schemes for 2D Scalar Conservation Laws," *Mathematics of Computation*, Vol. 45, No. 171, July 1985, pp. 15–21.